

Gate-Tunable Topological Flat Bands in Trilayer Graphene-Boron Nitride Moiré Superlattices

Bheema Lingam Chittari,^{1,2} Guorui Chen,² Yuanbo Zhang,³ Feng Wang,² and Jeil Jung^{1,2}

¹*Department of Physics, University of Seoul, Seoul 02504, Korea*

²*Department of Physics, University of California at Berkeley, Berkeley, CA 94709, USA*

³*Institute for Nanoelectronic Devices and Quantum Computing, Fudan University, Shanghai 200433, China*

We investigate the electronic structure of the flat bands induced by moiré superlattices and electric fields in nearly aligned ABC trilayer graphene-boron nitride interfaces where Coulomb effects can lead to correlated gapped phases. Our calculations indicate that valley-spin resolved isolated superlattice flat bands that carry a finite Chern number $C = 3$ proportional to layer number can appear near charge neutrality for appropriate perpendicular electric fields and twist angles. When the degeneracy of the bands is lifted by Coulomb interactions these topological bands can lead to anomalous quantum Hall phases that embody orbital and spin magnetism. Narrow bandwidths of ~ 10 meV achievable for a continuous range of twist angles $\theta \lesssim 0.6^\circ$ with moderate interlayer potential differences of ~ 50 meV make the TLG/BN systems a promising platform for the study of electric-field tunable Coulomb interaction driven spontaneous Hall phases.

PACS numbers: 73.22.Pr, 71.20.Gj, 31.15.aq

Generation of moiré superlattices in graphene and other 2D materials by forming van der Waals interfaces has emerged as an efficient route to tailor high quality artificial band structures [1–3]. In particular, the periodic moiré patterns in the length scale of a few tens of nanometers that arise due to small lattice constant mismatch or twist angles with the substrate give rise to moiré mini Brillouin zones whose zone corners are at energy ranges accessible by conventional field effects in gated transistor devices [4–10]. The interlayer coupling become effectively strong in the limit of long moiré pattern periods due to non-perturbative coupling between the superlattice zone folded moiré bands [4, 5], which are suggestive that flat bands can routinely form in the limit of long moiré pattern periods for a variety of 2D material combinations including twisted bilayer graphene and transition metal dichalcogenides heterojunctions [11–13]. Recent experiments have shown resistance peaks as a function of carrier doping indicative of Mott phases in twisted bilayer graphene at the first magic twist angle [14, 15] and in ABC trilayer graphene (TLG) nearly aligned with hexagonal boron nitride (BN) [16] when the Fermi energy is brought near the superlattice flat bands (SFB). In this work we carry out an analysis of the SFB in TLG/BN showing that they are generally topological bands, i. e. have finite Chern numbers, and the lifting of the valley-spin degeneracy by Coulomb interaction driven gaps of these Chern flat bands (CFB) can give rise to quantum anomalous Hall phases with orbital and spin magnetism even in the absence of an external magnetic field.

Model Hamiltonian— The model Hamiltonian for ABC stacked TLG is based on the low energy model for trilayer graphene with the band parameters obtained from density functional theory local density approximation (LDA) [17–19]. We represent the Hamiltonian acting in the basis of the low energy sites A for bottom and B for top layers. Each band is four-fold degenerate with two-fold degeneracy in the principal valleys (K, K') labeled with $v = \pm 1$, and two-fold degeneracy in real spin (\uparrow, \downarrow) labeled with $s = \pm 1$. We label the lowest valence and conduction (h, e) bands through $b = \pm 1$. The low

energy Hamiltonian for a rhombohedral N -layer graphene is

$$H_N^{v,\xi} = \frac{v_0^N}{(-t_1)^{N-1}} \begin{pmatrix} 0 & (\pi^\dagger)^N \\ \pi^N & 0 \end{pmatrix} + \Delta \sigma_z + H_N^R + H_\xi^M, \quad (1)$$

where $\pi = (vp_x + ip_y)$. We will discuss our results for $v = 1$ principal valley K unless stated otherwise. The parameter Δ represents an adjustable interlayer potential difference between the top and bottom layers that include the effects of a perpendicular electric field and its screening. In a TLG with $N = 3$ layers we model the remote hopping term corrections through

$$H_{3,v}^R = \left[\left(\frac{2v_0 v_3 p^2}{t_1} + t_2 \right) \sigma_x \right] + \left[\frac{2v_0 v_4 p^2}{t_1^2} - \Delta' + \Delta'' \left(1 - \frac{3v_0^2 p^2}{t_1^2} \right) \right] \mathbb{1}. \quad (2)$$

The effective hopping parameters are $t_0 = -2.62$ eV, $t_1 = 0.358$ eV, $t_2 = -0.0083$ eV, $t_3 = 0.293$ eV and $t_4 = -0.144$ eV [19, 20], where the associated velocities are defined as $v_m = \sqrt{3}a|t_m|/2\hbar$ with $a = 2.46\text{\AA}$ the lattice constant of graphene. The diagonal terms $\Delta' = 0.0122$ eV, and $\Delta'' = 0.0095$ eV are used to provide an accurate fit for the LDA bands. The moiré patterns have a period $\ell_M \simeq a/(\epsilon^2 + \theta)^{1/2}$ that depends on $\epsilon = (a - a_{BN})/a_{BN}$ the relative lattice constant mismatch between graphene and BN, and the twist angle θ . The moiré potential generated in graphene due to BN is given by

$$H_{\xi=\pm 1}^M(\vec{r}) = V_{A/B}^M(\vec{r}) = 2C_{A/B}\text{Re} \left[e^{i\phi_{A/B}} f(\vec{r}) \right] \frac{(\xi \sigma_z + \mathbb{1})}{2} \quad (3)$$

where the moiré parameters are $C_A = -14.88$ meV, $\phi_A = 50.19^\circ$ and $C_B = 12.09$ meV, $\phi_B = -46.64^\circ$ [4, 23], and the auxiliary function $f(\vec{r}) = \sum_{m=1}^6 e^{i\vec{G}_m \cdot \vec{r}} (1 + (-1)^m)/2$ is expressed using the six moiré reciprocal lattice $\vec{G}_{m=1\dots 6} = \hat{R}_{2\pi(m-1)/3} \vec{G}_1$ successively rotated by sixty degrees where $\vec{G}_1 = (0, 4\pi/(\sqrt{3}\ell_M))$. The parameter $\xi = \pm 1$ distinguishes the two types of possible alignments between TLG and BN

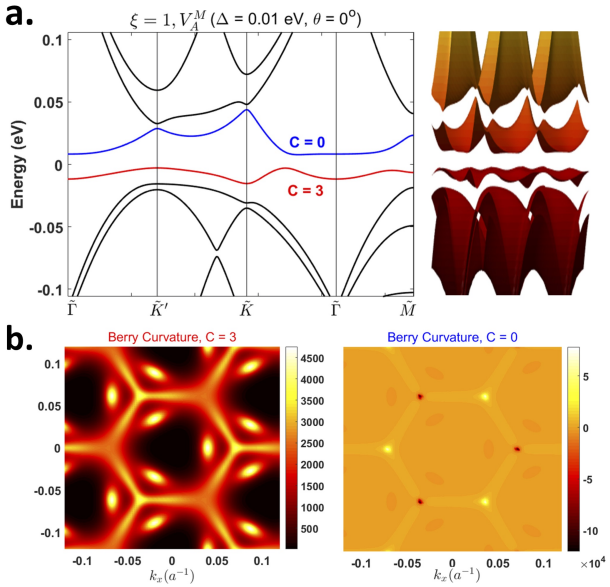


FIG. 1. (Color online) **a.** The band structure of ABC-TLG for zero twist angle near charge neutrality in the folded zones representation subject to $V_A^M = H_{\xi=1}^M$ moiré patterns and interlayer potential differences of $\Delta = 10$ meV that give rise to flat Chern bands with $C = 3$ represented in red and $C = 0$ trivial band represented in blue. **b.** The Berry curvatures for the valence and conduction band structures of panel (a) where we see Berry curvature hotspots near the trigonal warping band edges and mBZ zone boundaries that add up in the Chern band. In the trivial band we see sharp peaks with opposite Berry curvatures mainly at the mBZ that cancel out.

where we have defined the moiré pattern to perturb only the low energy A (bottom) or B (top) sites in the graphene layer contacting BN. The two moiré patterns will give rise to rather different flat band behaviors as a function of Δ and twist angle. These moiré pattern parameters given in sublattice basis can be related with pseudospin basis parameters $C_0 = -10.13$ meV, $\phi_0 = 86.53^\circ$, and $C_z = -9.01$ meV, $\phi_z = 8.43^\circ$ [4, 21].

Topological flat bands in TLG/BN superlattices— The presence of moiré superlattices can produce avoided gaps at the moiré mini Brillouin zone (mBZ) boundaries [21, 22, 24] while an additional gap at the primary Dirac point would isolate the low energy bands near charge neutrality [16, 23, 25]. Because the low energy bands in ABC trilayers are less dispersive than those of single or bilayer graphene, they are particularly suitable for the efficient isolation and narrowing of the low energy bands by electric fields that enhance both the primary and secondary gaps [16]. Here, we discuss how the gaps opened by perpendicular electric fields lead to Berry curvatures in the isolated flat bands of TLG/BN and can turn them into topological Chern bands with a quantized Hall effect. The Berry curvature for the n^{th} band can be calculated using the standard formula $\Omega_n(\vec{k}) = -2 \sum_{n' \neq n} \text{Im} \left[\langle u_n | \frac{\partial H}{\partial k_x} | u_{n'} \rangle \langle u_{n'} | \frac{\partial H}{\partial k_y} | u_n \rangle / (E_{n'} - E_n)^2 \right]$ [39] where for every k -point we take sums through all the

neighboring n' bands, the $|u_n\rangle$ are the moiré superlattice Bloch states and E_n are the eigenvalues. The Chern number of the n^{th} band is obtained from the Berry curvature through $C = \int d^2\vec{k} \Omega_n(\vec{k})/(2\pi)$ integrated in the Brillouin zone. Here we use an abbreviated notation $C = C_{v,s,N,\xi,b}$ with implicit valley, spin indices and other system parameters. In the band structures of TLG/BN in Fig. 1 we can clearly observe the primary gap near charge neutrality and secondary gaps near the mBZ boundaries as well as the Berry curvature hotspots that illustrate the distribution of Chern number weights, often near the mBZ boundaries where the secondary gaps open.

Our numerical calculations for TLG/BN predict the Chern numbers $C = \pm 3$ for the CFBs depending on system parameters. We have verified up to trilayers that

$$C = N v \xi \delta_{\text{sgn}(\Delta),\xi,b} \quad (4)$$

in an N -chiral graphene two dimensional electron gas (2DEG), where the Chern bands are found for either the valence or conduction bands depending on applied electric field sign and moiré pattern potential. In Fig. 2 we show that the calculated Chern numbers are quantized for a wide range of Δ values for valence and conduction bands of TLG/BN and BLG/BN. In particular we find that either the conduction or valence SFB near charge neutrality becomes a Chern band as soon as Δ opens a gap at the primary Dirac point. This behavior can be understood if we consider that a rhombohedral N -layer graphene [26] develops in the limit of small Δ a primary Chern weight $w_P \sim \text{sgn}(\Delta)bVN/2$ near each valley whose sign depends on $\text{sgn}(\Delta)$, the hole or electron band character $b = \pm 1$, as well as valley $v = \pm 1$ [27, 28, 32, 34]. In the absence of secondary gaps due to moiré patterns the K and K' principal valleys are mutually connected and the valley Chern numbers identified as Chern weights w_P near each valley are not protected topological numbers. Nevertheless, they give an intuitive idea about the Hall conductivity dynamics near the chiral 2DEG band edges and are useful for counting the number of zero-line modes in the valley Hall domain walls [30–37]. The situation is quite different when primary and secondary gaps are simultaneously present near the mBZ boundaries because the Chern weights sum $C^{e/h} = w_P^{e/h} + w_S^{e/h}$ needs to add up to a zero or finite integer value in each isolated band [38], where w_S^e or w_S^h are the secondary Chern weights for electron and hole bands. The secondary Chern weights near the mBZ boundaries depend on the moiré pattern potentials that generate the avoided secondary gaps, as evidenced by the fact that different moiré potentials V_A^M or V_B^M give rise to flat bands with different Chern numbers. The abrupt change in the band Chern number with the sign of Δ can be related with the sign changes of w_P . Considering that $w_P^h = -w_P^e$ for electrons and holes in the limit $|\Delta| \ll 1$ we conclude that the secondary weights should initially be equal $w_S^e = w_S^h$, see Fig. 2, while unequal electron-hole secondary Chern weights $w_S^e \neq w_S^h$ might be achievable using different moiré and Hamiltonian parameters. For increasing Δ the primary Chern weights are progressively pushed from the vicinity of Γ towards the mBZ boundaries closer to the

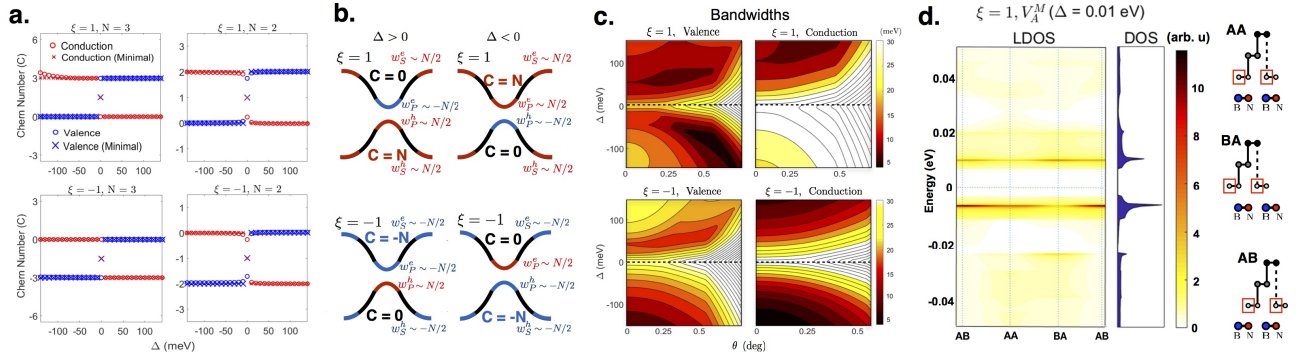


FIG. 2. (Color online) **a.** Chern numbers for the valence and conduction flat bands for aligned TLG on BN for the bands in Eqs. 1-2, bilayer on BN using H_2^R from Ref. 20 and corresponding minimal $H_\xi^R = 0$ models, calculated using a total of 18361 k -points in the mBZ. An abrupt transition happens when the sign of Δ changes near zero field. **b.** Schematic illustration of the Chern weights near $\tilde{\Gamma}$ and mBZ boundaries in the limit of $|\Delta| \ll 1$ that add up into an integer $C^e/h = w_P^e/h + w_S^e/h$, where $w_P^e = -w_P^h$ and $w_S^e = w_S^h$ so that either the electron or hole band has a finite Chern number. **c.** Bandwidth phase diagram for the valence and conduction bands as a function of interlayer potential difference Δ and twist angle θ calculated from the difference between the maximum and minimum eigenvalue within a band. **d.** Local stacking and energy dependent LDOS and DOS manifesting the localization of flatband wavefunctions.

location of the secondary weights $w_S^{e/h}$ while maintaining a constant Chern number in the isolated bands. Conclusions similar to our analysis in TLG/BN could be expected in other rhombohedral-multilayer graphene N -chiral 2DEGs, although the remote hopping terms in the band Hamiltonian are important to properly account for the flatband dispersions and the secondary gaps. The Supplemental material Figs. S1-S2 for the Berry curvatures in minimal N -chiral multilayer graphene with $N=1,2,3$ illustrates the evolution of Chern weight distribution in the mBZ from small to large Δ .

Field-dependent bandwidths and localization- The external electric field strength modulates the size of the primary band gap near $\tilde{\Gamma}$ which impacts directly the shape of the low energy SFB and their optimum flatness will depend on field direction and strength. The non-monotonic behavior of the band flatness as a function of electric field strength highlights the electron-hole asymmetry inherent in TLG and the relevance of the moiré potential details in determining the band shapes. In Fig. 2 we represent a colormap that summarizes the evolution of the bandwidth of the SFB as a function of electric field and twist angle quantified through the difference between the maximum and minimum energy values within a given band. We can observe that for every given twist angle there is often an optimum interlayer potential difference that maximizes the band flatness either for positive and negative field directions, and that the overall flatness does not always grow monotonically with increasing electric field magnitude. Increasing Δ to appropriately large values will favor the onset of Coulomb interaction driven gaps by increasing the separation of the SFB with neighboring energy bands and reducing its bandwidth. In addition to the electric field magnitude and direction, the relative twist angle in the system has an impact in the flatness and energy location of the SFB. Introducing a finite twist angle is expected to widen the moiré bands due to the increase in the size of the mBZ in reciprocal space for reduced moiré real space periods. However, for relatively small twist angle values of up to $\sim 1^\circ$ the moiré pattern periods are still

~ 10 nm and the enhanced suppression of achievable bandwidth through external electric fields can sufficiently compensate for this bandwidth increase due to rotation. Direct information on the band flatness is reflected in the density of states (DOS) plots as a function of energy allowing to find the energy regions where Coulomb correlations are expected to be stronger. The local density of states (LDOS) plots for every local stacking configuration also provides insights on the electron localization properties of the SFB electrons in real space, see Fig. 2. Charge and spin density modulations are expected to take place mainly around the LDOS peaks when the degeneracy of the bands is lifted due to Coulomb interactions. The LDOS plots provide valuable information for guiding scanning probe microscopy experiments that search for flat band signatures.

Spontaneous quantum Hall phases— Filling of nontrivial Chern bands will lead to an associated quantum Hall effect that should be observable in transport experiments. An interesting scenario is found in partially filled CFB when valley and spin degeneracy is lifted by Coulomb interactions giving rise to a variety of spontaneous quantum Hall phases. We take as a working assumption that the interaction driven gapped states at 1/4, 1/2, 3/4 partial filling of the flat bands will develop into spin-collinear and valley-collinear phases where each valley-spin flavor can be filled sequentially. In the Hartree-Fock approximation it is reasonable to assume that same spin polarization will be preferred over non-collinear spin states as in conventional quantum Hall ferromagnetism of Landau levels [40], while valley polarized phases can be preferred due to momentum space exchange condensation over valley-coherent phases with two partially filled valleys [41]. We represent Coulomb interaction driven gaps through rigid shifts proportional to λ in the CFB energies through a function $g(v,s)$ to classify the different possible states assuming any of them are possible. We will follow a classification scheme closely similar to the four valley-spin components of N -chiral multilayer graphene in Refs. [28, 29], in

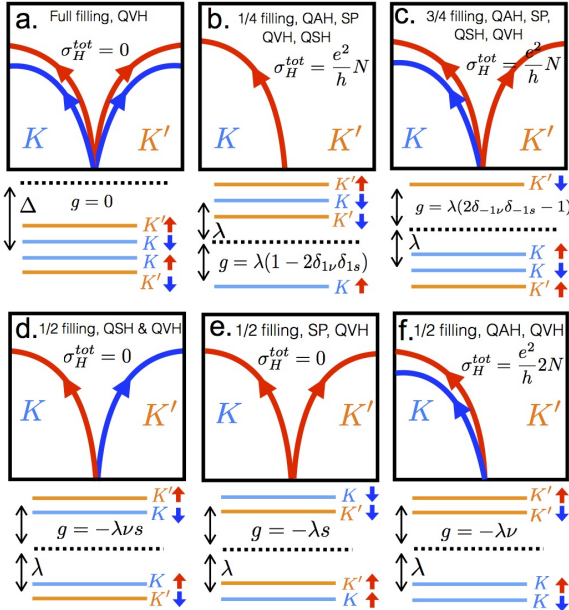


FIG. 3. (Color online) For the valence flat bands associated with $\Delta > 0$ and $\xi = 1$ moiré potentials we schematically represent how the occupation of valley (K, K') and spin (\uparrow, \downarrow) resolved CFB contributes towards the generation orbital and spin magnetism. Four different configurations of valley spin are possible for 1/4, 3/4 filling (b.-c.), and two per each 1/2 filling represented (d.-f.). The total charge Hall conductivity $\sigma_H^{tot} = \sum_i \sigma_H^i$ of the bands is contributed by $\sigma_H^i = C_i e^2/h$ for each occupied valley-spin flavor i where $C_i = N \nu \xi \delta_{sgn(\Delta), \xi, b}$, and the valley Hall conductivity is proportional to filling. A variety of spontaneous quantum anomalous, valley and spin Hall effects should be expected when interaction driven gaps open for 1/4, 1/2, 3/4 filling of the CFB. In particular 1/4 and 3/4 fillings are found to simultaneously have spin and orbital magnetism.

TABLE I. Summary of the Chern flat band configurations (1 for occupied, 0 for unoccupied) and corresponding charge, spin, and valley Hall conductivities (in e^2/h units) and insulator types: quantum anomalous Hall (QAH), spin Hall (QSH), valley Hall (QVH), and spin polarized (SP). The layer number $N = 3$ is equal to the flatband Chern number magnitude in TLG/BN.

Fig.	$K \uparrow$	$K \downarrow$	$K' \uparrow$	$K' \downarrow$	$\sigma^{(CH)}$	$\sigma^{(SH)}$	$\sigma^{(VH)}$	Insulator
3(a)	1	1	1	1	0	0	$4N$	QVH
3(b)	1	0	0	0	N	0	N	QAH, SP, QVH
3(c)	1	1	1	0	N	$-N$	$3N$	QAH, QSH, SP, QVH
3(d)	1	0	0	1	0	$2N$	$2N$	QSH, QVH
3(e)	1	0	1	0	0	0	$2N$	SP, QVH
3(f)	1	1	0	0	$2N$	0	$2N$	QAH, QVH

our case facilitated by the fact that the quantum valley Hall effect is proportional to CFB filling. In Fig. 3 we illustrate the example of $b = 1$, $\xi = 1$, $\Delta > 0$ case corresponding to the top panel of Fig. 1 a representative selection of quantum Hall ground states also summarized in Table I. At charge neutrality when all CFB are filled at filling 1 we have a valley Hall state where the charge Hall conductivity summed over

all occupied flavors totals to zero the charge Hall conductivity is $\sigma_H^{tot} = \sum_i \sigma_H^i = 0$. The cases of 1/4 and 3/4 filling can be pictured through selective filling/emptying of a given (v', s') band using shifts of $g(v, s) = \lambda (1 - 2\delta_{v'v} \delta_{s's})$ and $\lambda (2\delta_{v'v} \delta_{s's} - 1)$ respectively. These are interesting cases with $\sigma_H^{tot} = \pm Ne^2/h$ charge Hall conductivity where we have simultaneously a quantum anomalous and spin Hall effect. For the 1/2 filling when two CFB are filled we have a greater variety of quantum Hall ground states. One of the possibilities is the quantum anomalous Hall phase where two equal v' valley CFBs are filled. The shift functions can then be modeled through $g(v, s) = \lambda (1 - 2\delta_{v'v})$ and the charge Hall conductivity is $\sigma_H^{tot} = 2Nv'e^2/h$. The remaining two scenarios have Hall conductivity $\sigma_H^{tot} = 0$, in the case where the same spin s' are polarized and are modeled through $g(v, s) = \lambda (1 - 2\delta_{s's})$ shifts, and the quantum spin phase can be modeled through $g(v, s) = \pm \lambda vs$ shifts depending on the relative signs of the occupied valley-spin indices.

Discussions— In this work we have analyzed the topological character of the superlattice flat bands (SFB) in ABC trilayer graphene-hexagonal boron nitride superlattices where signatures of gate tunable Mott gaps have been observed recently in experiments [16]. Our analysis indicates that topological flat bands with Chern number $C = \pm 3$ will form either for electrons or holes depending on the electric field sign and moiré potential. This scenario makes it possible to study Coulomb interaction driven ordered phases in zero and finite Chern number flatbands within the same device by modifying the carrier density from electrons to holes, making this system an interesting platform for exploring the interplay of correlation physics with topological order. Band gap openings for partial filling of the flat bands indicate that a selective occupation of Chern flat bands (CFB) of different valley-spin flavors should be possible. Assuming valley-spin collinear ground states of these partially filled CFB, different types of spontaneous quantum Hall phases with orbital and spin magnetization can be expected, with total charge Hall conductivities of zero or $\sigma_H^{tot} = \pm 6e^2/h$ expected for 1/2 filling, whereas $\sigma_H^{tot} = \pm 3e^2/h$ that is always finite is expected for 1/4 or 3/4 filling. From a device application point of view, one important advantage of the field tunable gapped Dirac materials is that the bandwidth variations of the SFB are less sensitive to twist angle compared to twisted bilayer graphene where a precise twist angle control is required.

Acknowledgments— We thank A. H. MacDonald for helpful discussions. The initial idea and proof of principle calculation of 2D flatband engineering was supported by an ARO MURI award (W911NF- 15-1-0447). Y.Z. acknowledge financial support from National Key Research Program of China (2016YFA0300703), and NSF of China (grant nos. U1732274, 11527805 and 11425415). Support from the Korean NRF is acknowledged for B.L.C. through NRF-2017R1D1A1B03035932 and J.J. through NRF-2016R1A2B4010105.

Note added: During the finalization of this manuscript we became aware of a related recent work [42].

-
- [1] B. Hunt, J. D. Sanchez-Yamagishi, A. F. Young, M. Yankowitz, B. J. LeRoy, K. Watanabe, T. Taniguchi, P. Moon, M. Koshino, P. Jarillo-Herrero, and R. C. Ashoori, *Science* **340**, 1427 (2013).
- [2] C. R. Dean, L. Wang, P. Maher, C. Forsythe, F. Ghahari, Y. Gao, J. Katoch, M. Ishigami, P. Moon, M. Koshino, T. Taniguchi, K. Watanabe, K. L. Shepard, J. Hone, and P. Kim, *Nature* **497**, 598 (2013).
- [3] L. A. Ponomarenko, R. V. Gorbachev, G. L. Yu, D. C. Elias, R. Jalil, A. A. Patel, A. Mishchenko, A. S. Mayorov, C. R. Woods, J. R. Wallbank, M. Mucha-Kruczynski, B. A. Piot, M. Potemski, I. V. Grigorieva, K. S. Novoselov, F. Guinea, V. I. Fal'ko, and A. K. Geim, *Nature* **497**, 594 (2013).
- [4] J. Jung, A. Raoux, Z. Qiao, and A. H. MacDonald, *Phys. Rev. B* **89**, 205414 (2014).
- [5] R. Bistritzer and A. H. MacDonald, *Proc. Natl. Acad. Sci. U.S.A.* **108**, 12233 (2011).
- [6] G. Li, A. Luican, J. L. Dos Santos, A. C. Neto, A. Reina, J. Kong, and E. Andrei, *Nat. Phys.* **6**, 109 (2010).
- [7] J. R. Wallbank, A. A. Patel, M. Mucha-Kruczynski, A. K. Geim, and V. I. Fal'ko, *Phys. Rev. B* **87**, 245408 (2013).
- [8] J. M. B. Lopes dos Santos, N. M. R. Peres, and A. H. Castro Neto, *Phys. Rev. Lett.* **99**, 256802 (2007).
- [9] P. Moon and M. Koshino, *Phys. Rev. B* **85**, 195458 (2012).
- [10] M. Yankowitz, J. Xue, D. Cormode, J. D. Sanchez-Yamagishi, K. Watanabe, T. Taniguchi, P. Jarillo-Herrero, P. Jacquod, and B. J. LeRoy, *Nat. Phys.* **8**, 382 (2012).
- [11] F. Wu, T. Lovorn, E. Tutuc, A. H. MacDonald, arXiv:1804.03151 (2018).
- [12] Y. Pan, S. Folsch, Y. Nie, D. Waters, Y-C Lin, B. Jariwala, K. Zhang, K. Cho, J. A. Robinson, and R. M. Feenstra, *Nano Lett.* **18**, 1849-1855 (2018).
- [13] S. Carr, D. Massatt, M. Luskin, E. Kaxiras, arXiv:1803.01242 (2018).
- [14] Y. Cao, V. Fatemi, A. Demir, S. Fang, S. L. Tomarken, J. Y. Luo, J. D. Sanchez-Yamagishi, K. Watanabe, T. Taniguchi, E. Kaxiras, R. C. Ashoori, and P. Jarillo-Herrero, *Nature* **556**, 80-84 (2018).
- [15] Y. Cao, V. Fatemi, S. Fang, K. Watanabe, T. Taniguchi, E. Kaxiras, and P. Jarillo-Herrero, *Nature* **556**, 43-50 (2018).
- [16] G. Chen, L. Jiang, S. Wu, B. Lv, H. Li, K. Watanabe, T. Taniguchi, Z. Shi, Y. Zhang, F. Wang, arXiv:1803.01985 (2018).
- [17] F. Zhang, B. Sahu, H. K. Min, and A. H. Macdonald, *Phys. Rev. B* **82**, 035409 (2010).
- [18] M. Koshino, E. McCann, *Phys. Rev. B* **80**, 165409 (2009).
- [19] Unpublished.
- [20] J. Jung and A. H. MacDonald, *Phys. Rev. B* **89**, 035405 (2014).
- [21] J. Jung, E. Laksono, A. M. DaSilva, A. H. MacDonald, M. Mucha-Kruczynski, and S. Adam, *Phys. Rev. B* **96**, 085442 (2017).
- [22] A. M. DaSilva, J. Jung, S. Adam, and A. H. MacDonald *Phys. Rev. B* **91**, 245422 (2015).
- [23] J. Jung, A. M. DaSilva, A. H. MacDonald, and S. Adam, *Nat. Commun.* **6:6308** (2015).
- [24] E. Wang et al. *Nat. Phys.* **12**, 1111 (2016).
- [25] J. C. W. Song, P. Samutpraphoot, and L. S. Levitov, *Proc. Nac. Acad. Sci.* **112** 10879-10883 (2015).
- [26] H. Min and A. H. MacDonald, *Prog. Theo. Phys. Supp.* **176**, 227-252 (2008).
- [27] D. Xiao, W. Yao, Q. Niu, *Phys. Rev. Lett.* **99**, 236809 (2007).
- [28] F. Zhang, J. Jung, G. A. Fiete, Q. Niu, and A. H. MacDonald, *Phys. Rev. Lett.* **106**, 156801 (2011).
- [29] J. Jung, F. Zhang, and A. H. MacDonald *Phys. Rev. B* **83**, 115408 (2011).
- [30] G. E. Volovik, *The Universe in a helium droplet*, Int. Ser. Monogr. Phys. 117 (2006).
- [31] I. Martin, Y. M. Blanter, A. F. Morpurgo, *Phys. Rev. Lett.* **100**, 036804 (2008).
- [32] J. Jung, F. Zhang, Z. Qiao, and A. H. MacDonald, *Phys. Rev. B* **84**, 075418 (2011).
- [33] C. Lee, G. Kim, J. Jung, H. Min, *Phys. Rev. B* **94**, 125438 (2016).
- [34] J. Jung, Z. Qiao, Q. Niu, and A. H. MacDonald, *Nano Lett.*, **12**, 2936-2940 (2012).
- [35] J. Li, K. Wang, K. J. McFaul, Z. Zern, Y. Ren, K. Watanabe, T. Taniguchi, Z. Qiao, and J. Zhu, *Nature Nanotechnology* **11**, 1060-1065 (2016).
- [36] F. Zhang, A. H. MacDonald, E. Mele, *Proc. Nac. Acad. Sci.* **110** 10546-10551 (2013).
- [37] L. Ju, Z. Shi, N. Nair, Y. Lv, C. Jin, J. Velasco Jr, C. Ojeda-Aristizabal, H. A. Bechtel, M. C. Martin, A. Zettl, J. Analytis, F. Wang, *Nature* **520**, 650-655 (2015).
- [38] M. Z. Hasan and C. L. Kane *Rev. Mod. Phys.* **82**, 3045 (2010).
- [39] D. Xiao, M.-C. Chang, and Q. Niu, *Rev. Mod. Phys.* **82**, 1959 (2010).
- [40] R. E. Prange and S. M. Girvin (ed) 1990 *The Quantum Hall Effect 2nd edn* (Berlin: Springer).
- [41] J. Jung, M. Polini, and A. H. MacDonald, *Phys. Rev. B* **91**, 155423 (2015).
- [42] Y.-H. Zhang, D. M., Y. C., P. Jarillo-Herrero, T. Senthil, arXiv:1805.08232v1.

Supplemental Material

In this supplement we present band structures and Berry curvatures that are obtained for the minimal band Hamiltonian for trilayer, bilayer and monolayer graphene on boron-nitride modeled by Eq. 1 in the main text setting the remote hopping terms to zero $H_N^R = 0$ and subject to sublattice selective moiré potentials H_ξ^M labeled with $\xi = \pm 1$. We present results for the Berry curvatures in the limit of small $\Delta = \pm 0.0001$ and moderately large $\Delta = 0.1$ eV are clearly shown in the Fig. S1 and S2 respectively to illustrate the distribution of the Chern weights depending on primary gap size. The Fig. S1 shows the Berry curvatures alone for small gaps, whereas the Fig. S2 shows the band structures together with the berry curvatures for the larger gaps where we can visualize the redistribution of the Chern weights. Fig. S3 illustrates the band structure and Berry curvatures of graphene on boron nitride subject to realistic moiré patterns from (PRB 89, 205414 (2014)) that include both the diagonal terms and off-diagonal components, plus an *ad hoc* gap at the primary Dirac point to verify the formation of isolated bands.

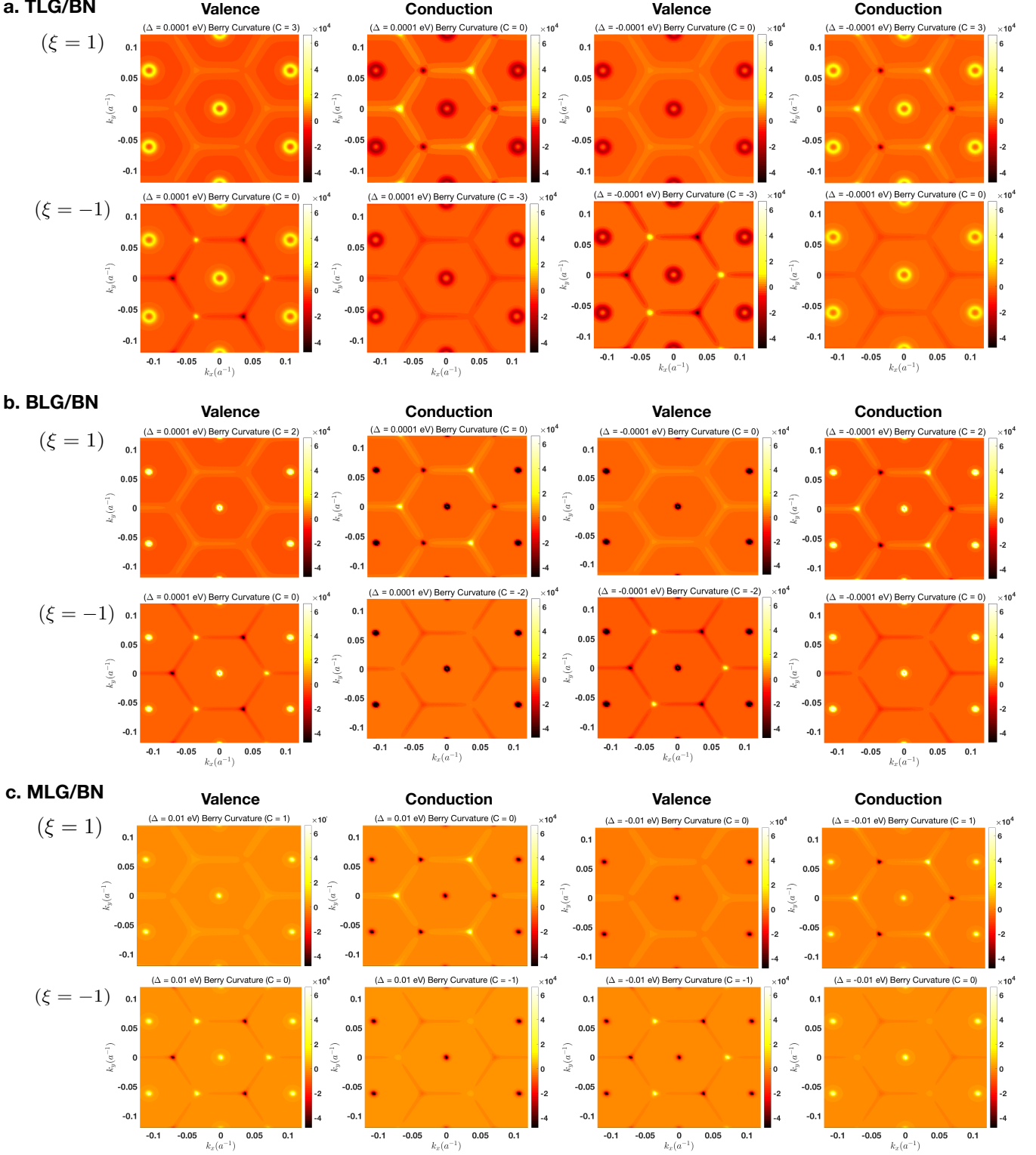


FIG. 4. (Color online) The Berry curvatures of ABC-TLG (**a.** **TLG/BN**), bilayer (**b.** **BLG/BN**) and monolayer (**c.** **MLG/BN**) peaked near $\bar{\Gamma}$ in the limit of small interlayer potential differences Δ associated to the valence band (left) and conduction bands (right) near charge neutrality of rhombohedral N -chiral graphene on BN modeled by Eq. 1 in the main text for $N=3,2,1$ with $H_N^R = 0$ subject to $V_A^M = H_{\xi=1}^M$ (top row) and $V_B^M = H_{\xi=-1}^M$ (bottom row) sublattice selective moiré patterns. **a.** Berry curvatures for valence and conduction flat bands for TLG/BN obtained for small interlayer potential differences of $\Delta = \pm 0.0001$ eV giving rise to flat Chern bands with $C = \pm 3$ and superlattice flat bands with $C = 0$. **b.** The Berry curvatures associated to bilayer BLG/BN with $\Delta = \pm 0.0001$ eV subject to $\xi = \pm 1$ moiré potentials giving rise to superlattice flat bands with $C = \pm 2$ and $C = 0$. **c.** The Berry curvatures associated to monolayer MLG/BN with $\Delta = \pm 0.01$ eV subject to sublattice selective $\xi = \pm 1$ moiré potentials giving rise to superlattice flat bands with $C = \pm 1$ and $C = 0$.

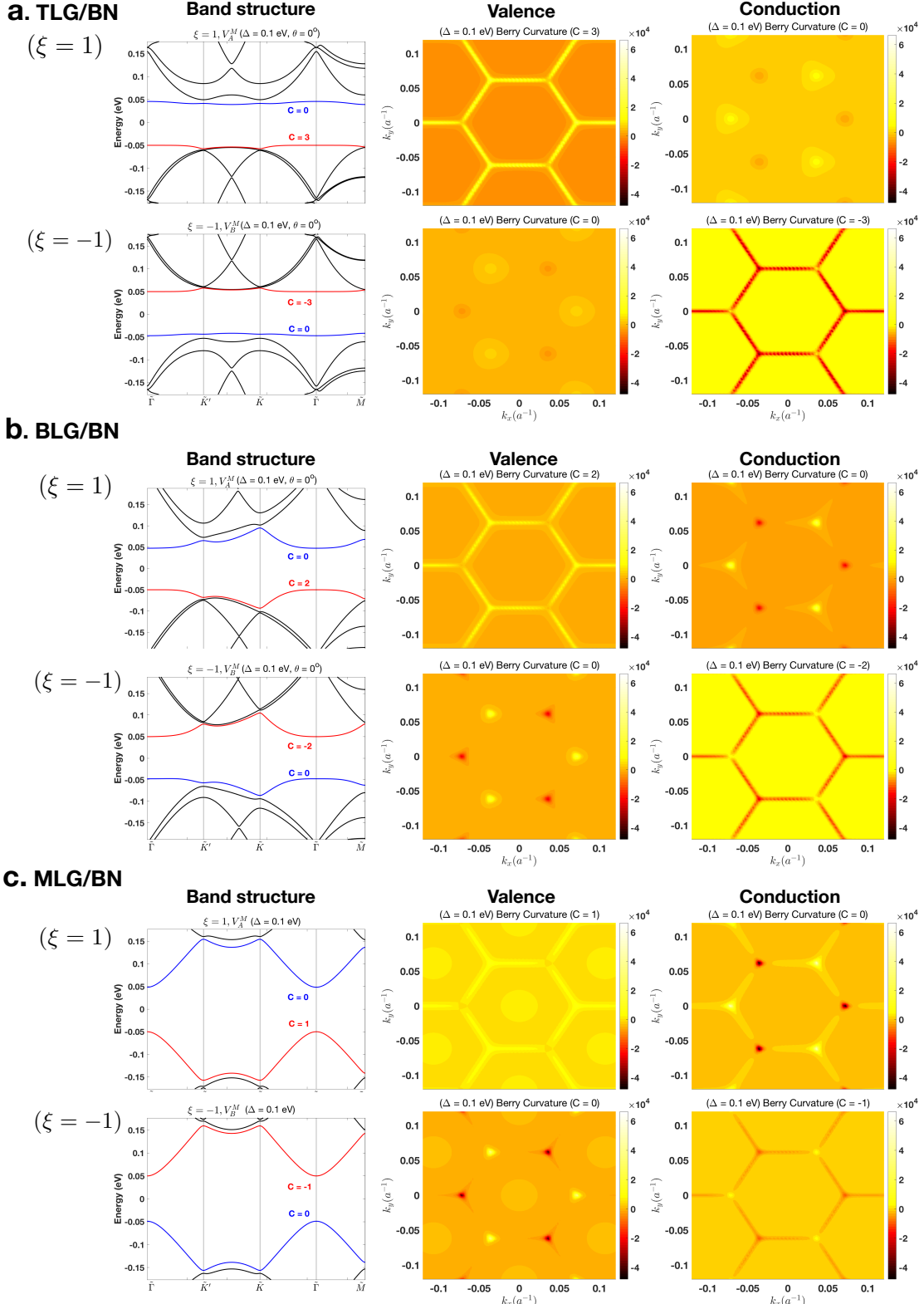


FIG. 5. (Color online) The band structure of ABC-TLG (**a.** **TLG/BN**), bilayer (**b.** **BLG/BN**) and monolayer (**c.** **MLG/BN**) calculated using the minimal model without remote hopping terms (Eq. 1 in main text with $H_N^R = 0$) for zero twist angle, subject to $V_A^M = H_{\xi=1}^M$ and $V_B^M = H_{\xi=-1}^M$ moiré patterns and interlayer potential differences of $\Delta = 0.1$ eV that give rise to flat Chern bands with $C = \pm 3$, for TLG/BN, $C = \pm 2$, for BLG/BN, and $C = \pm 1$ for MLG/BN. The Chern bands represented in red and the trivial $C = 0$ bands are represented in blue. We also plot the Berry curvatures associated to the valence and conduction bands where we can observe how the Chern weights are pushed towards the mBZ boundaries.

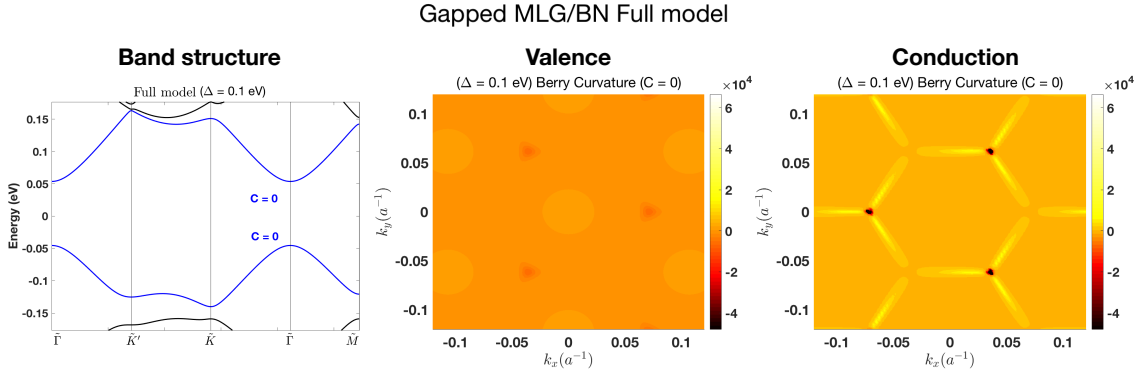


FIG. 6. (Color online) The band structure of the MLG/BN model with full moiré pattern potential including diagonal and off-diagonal terms (PRB 89, 205414 (2014)) plus a primary gap $\Delta = 0.1$ eV that leads to isolated valence and conduction bands with zero Chern number. The Berry curvatures for the valence and conduction bands show peaks near the mBZ boundaries and zone corners that cancel each other.